# Correcting Current-Induced Magnetometer Errors on UAVs: An Online Model-Based Approach

Matthew Silic and Kamran Mohseni, *Senior Member, IEEE*

***Abstract*—The yaw attitude of an unmanned aerial vehicle (UAV) is important for navigation applications. Magnetometers are attractive because they can directly resolve the yaw attitude of the UAV. Roboticists, however, often dismiss magnetometers because of the instrument's susceptibility to unwanted magnetic sources, such as hard irons, soft irons and electric currents generated by the UAV's powertrain. Dynamic current-induced magnetometer biases are especially hard to fix because of their time dependency. A hardware fix is to isolate or shield the current carrying wires of the powertrain from the magnetometer. However, for UAVs with weight and space restrictions, this solution may not be feasible. An alternative is to fix the errors using software. This work takes the software approach. Specifically, a model for the current-induced magnetometer bias as a function of the throttle command is established. Based on this model, an adaptive estimator is developed that determines the model parameters in realtime. The advantage of our method over existing techniques is the ability to handle rapid changes in throttle command, thanks to the inclusion of the bias model. Experiments show the estimator can compensate for the current-induced magnetometer bias across all throttle settings and yaw angles.**

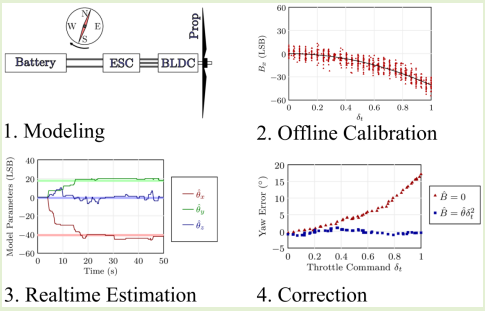


***Index Terms*—Magnetic sensors, parameter estimation, calibration.**

## I. Introduction

THE magnetic compass was first discovered over 2000 years ago. By the 14th century, mariners had come to rely on the magnetic compass for navigation [1]. To this day, compasses are used to give orientation. Digital compasses, or magnetometers, can be commonly found on robotic platforms and smartphones. A three-axis magnetometer, when paired with a three-axis accelerometer, can resolve the three-axis attitude of a robotic platform [2]. While this functionality is attractive, many roboticists forgo the use of magnetometers completely [3]. This is because magnetometers are heavily influenced by unwanted magnetic sources. However, with proper calibration, magnetometers can be successfully deployed on a robotic platform.

Many methods of magnetometer calibration can be found in the literature [4]–[10]. The cited methods are similar in that the calibration parameters are determined solely from magnetometer measurements. That is, no additional sensor is needed. However, as proved in [7], these "autocalibration" methods are unable to correct for misalignment between the magnetometer and other inertial sensors. As shown in [8], misalignment is detrimental to attitude estimation. In order to correct for magnetometer misalignment, additional sensors must be used, such as gyroscopes [11], [12], accelerometers [13], [14], or cameras [15].

The effect of current carrying wires on magnetometers in unmanned aerial vehicle (UAV) applications has been previously reported. System identification techniques are reported in [16], [17]. Both papers characterize the magnetic bias caused by driving the electric motors of a quad-copter. In [16], a bivariate polynomial is fit to the amplitude of the magnetic

Manuscript received August 26, 2019; revised September 24, 2019; accepted September 25, 2019. Date of publication October 2, 2019; date of current version December 31, 2019. This work was supported in part by the Office of Naval Research (ONR) and NSF. The associate editor coordinating the review of this article and approving it for publication was Prof. Tarikul Islam. *(Corresponding author: Kamran Mohseni.)*

M. Silic is with the Department of Mechanical and Aerospace Engineering, University of Florida, Gainesville, FL 32611 USA (e-mail: msilic@ufl.edu).

K. Mohseni is with the Department of Mechanical and Aerospace Engineering, University of Florida, Gainesville, FL 32611 USA, with the Department of Electrical and Computer Engineering, University of Florida, Gainesville, FL 32611 USA, and also with the Institute for Networked Autonomous Systems, University of Florida, Gainesville, FL 32611 USA (e-mail: mohseni@ufl.edu).

Digital Object Identifier 10.1109/JSEN.2019.2945201

bias. In [17], a local linear model is fit to each component of the magnetic bias. An online method of determining the magnetic bias is given in [18]. The authors, however, assume the magnetic bias is constant.

In this work, we seek to cancel the magnetometer bias induced by current carrying wires located in the magnetometer's vicinity. This work is different from previous work in that we determine the model for the current-induced magnetometer bias through deduction, as opposed to induction. That is, we deduce the relationship between throttle command and magnetometer bias using physical models of the UAV's powertrain. This work also derives a new estimator that is able to determine the magnetometer bias in realtime. The proposed estimator is able to handle time varying biases, thanks to the inclusion of the bias model. We consider the injection of throttle information into the adaptive bias estimator to be the primary contribution of this work.

Existing adaptive estimators assume the bias is constant [18], [19]. Thus, a change in throttle would shift the equilibrium point of the estimator. However, because we are estimating a set of model parameters (as opposed to the bias directly), our approach can handle rapid changes in the throttle command. Furthermore, the quasi-static assumption is more applicable to a set of model parameters than to the bias itself.

The remainder of this manuscript is organized as follows. Section II reviews magnetometer calibration for time-invariant errors, deduces a model for the current-induced bias, proposes a nonlinear adaptive estimator to determine the model parameters, and describes the hardware/implementation. Section III presents the experimental results. Section IV interprets the results, states our conclusions, and discusses some practical applications of this work.

## II. Methods & Materials

This section documents the methods and materials employed in this study. First, the sensor calibration problem is stated. An existing calibration method is reviewed, followed by our adaptation of the method in order to permit *in-situ* magnetometer calibration. Next, a model for the current-induced bias is established by combining knowledge of eletromagnetism, electric motors, and propeller aerodynamics. Following this, an adaptive estimator is designed in order to determine the model parameters in realtime. Finally, the hardware is described, along with how the algorithm is implemented.

### A. Basic Sensor Calibration

Magnetometers are affected by typical instrument errors: scaling factors, nonorthogonality, misalignment and biases. Magnetometers are also subject to *artificial* errors, *i.e.* errors caused not by the instrument but by magnetic distortions. These errors are classified as hard irons or soft irons. "Hard iron" denotes an unwanted magnetic source, such as permanent magnets or current carrying wires. A hard iron produces the same magnetic field, no matter how it is orientated with respect to the Earth's magnetic field. "Soft iron" denotes a magnetic distortion that depends on the incidence angle of the Earth's magnetic field. Steel is an example of a soft iron. The magnetometer measures the superposition of the Earth's magnetic field and any artificial errors. The purpose of magnetometer calibration is to extract the Earth's magnetic field vector from the sensor's output, which is corrupted by instrument errors and artificial errors.

Let $\vec{u} \in \mathbb{R}^3$ be the sensor's input and let $\vec{v} \in \mathbb{R}^3$ be the sensor's output. A general error model for a tri-axial field sensor is given by [20]

$$\vec{v} = K\vec{u} + \vec{b}, \tag{1}$$

where the distortion matrix $K \in \mathbb{R}^{3\times3}$ includes all errors proportional to the sensor inputs and $\vec{b} \in \mathbb{R}^3$ includes all errors that are attitude-independent. Equation (1) models all linear and time-invariant sensor errors, including instrument errors and artificial errors. Solving (1) for $\vec{u}$ yields

$$\vec{u} = L\vec{v} - \vec{d} \tag{2}$$

where $L \equiv K^{-1}$ and $\vec{d} \equiv K^{-1}\vec{b}$. Thus, the sensor calibration problem is mathematically equivalent to determining $L$ and $\vec{d}$. Once $L$ and $\vec{d}$ have been acquired, $\vec{u}$ may be recovered from $\vec{v}$ using (2).

The literature is replete with calibration methods; a method that is both simple and effective is the Dot Product Invariance (DPI) method presented in [20]. The DPI method is simple because it can be solved using least squares. It is effective because it corrects for sensor misalignment, a necessary correction if the magnetometer is to be used for navigation. Other methods that account for magnetometer misalignment can be found in [13], [14]. However, these methods are more complicated than the DPI method. And like the DPI method, they rely on additional sensors.

The DPI method exploits the fact that the dot product between two vectors is invariant under rotations. Thus, given a reference vector $\vec{w}$, the dot product $\vec{w} \cdot \vec{u}$ is

$$\vec{w} \cdot \vec{u} = \vec{w}^T\vec{u} = \vec{w}^T L\vec{v} - \vec{w}^T\vec{d} = \text{const.} \tag{3}$$

This equation is linear-in-the-parameters. Thus, all 12 elements in $L$ and $\vec{d}$ may be estimated using least squares. The only stipulation is that $\vec{w}$ cannot be parallel or perpendicular to the field vector $\vec{u}$.

The DPI method requires many observations of the reference vector. The accuracy of the resulting calibration depends on the accuracy of the reference vector. Assuming the magnetometer is packaged together with an accelerometer, a convenient reference vector is the down direction as measured by the accelerometer. However, there are two problems with using an accelerometer. First, the accelerometer itself needs to be calibrated. Second, the sensor must be stationary so that inertial accelerations do not corrupt the accelerometer's measurement of the gravitational field.

An alternative to using an accelerometer is to use a calibration cube [21], [22]. Based on which face of the cube is pointing upward, the reference downward direction may be inferred. However, there are two problems with using a calibration cube. First, the process is tedious. Second, the resulting calibration is only valid for when the magnetometer is in the cube. Once the magnetometer is mounted in the vehicle, magnetic sources on the vehicle will throw off the calibration.

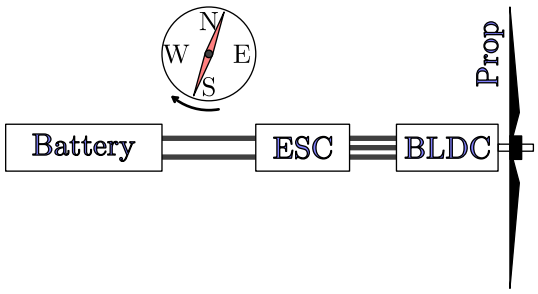


Fig. 1. The UAV's powertrain consists of a LiPo battery, an electronic speed controller (ESC), a brushless DC motor (BLDC), and a propeller. The motor, via the ESC, draws current from the battery. This current produces a magnetic field which interferes with the nearby magnetometer.

Through trial and error, the authors found a reliable source for the reference vector. Here, we propose to use the downward direction as estimated by an attitude estimator. The attitude is estimated using the nonlinear observer developed by Mahony, et al. in [23]. The Mahony filter fuses gyroscope and accelerometer readings to maintain an accurate earth-to-body rotation matrix, $R_e^b$. Assuming a north-east-down (NED) coordinate system is fixed to the earth's reference frame, it is easy to show the necessary reference vector is simply the last column of $R_e^b$.

There are three advantages for using the third column of the rotation matrix. First, because the reference vector is fused from gyroscope and accelerometer readings, the vector is less sensitive to errors in the accelerometer. Second, because the reference vector is extracted from an orthonormal matrix, the vector is automatically normalized. Finally, because the reference vector is measured using the onboard IMU, the calibration can be performed by rotating the vehicle by hand. The third advantage is particularly important, since it is imperative for the magnetometer to be calibrated in its final configuration on the vehicle.

### B. Modelling the Magnetometer Bias

The goal is to establish the transfer function between the throttle command, $\delta_t$, and the current-induced magnetometer bias, $\vec{B}$. Our approach is to analyze the various components of the powertrain (Fig. 1). Once the transfer functions of the various components are established, the desired transfer function directly follows.

*1) Magnetic Disturbance:* The magnetic field produced by a current carrying wire at a point $P$ is given by the Biot-Savart law [p. 889] [24]

$$\vec{B} = \frac{\mu_0 I}{4\pi} \int \frac{d\vec{s} \times \vec{r}}{r^3}, \tag{4}$$

where $\mu_0$ is the permeability of free space, $\vec{r}$ is the position of $P$ with respect to a differential current element $I\,d\vec{s}$, and $r$ is the magnitude of $\vec{r}$. Our purpose is not to solve (4) but to realize the magnetic field induced by the current carry wire is proportional to the current. Furthermore, the proportionality constant depends on the path of the wire.

*2) Motor/ESC:* An electric motor converts electrical power into mechanical power. The electrical portion and the mechanical portion of the motor are coupled magnetically.

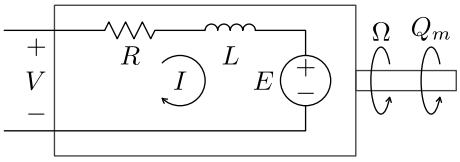


Fig. 2. Equivalent circuit for a brushed DC motor.

The magnetic coupling is realized through the armature and field. The armature refers to one or more current carrying copper windings. The field refers to a magnetic field that is produced by a permanent magnet or another winding.

Brushed DC motors have the armature wound on the rotor and the field fixed to the stator. When current is pushed through the armature, the field produces a torque on the rotor, as described by the Lorentz force law. In order for the rotor to rotate continuously, the current in the winding must change directions every half-turn of the rotor [p. 876] [24]. The process of switching the direction of the current is called commutation. On a brushed DC motor, commutation is done mechanically using a pair of graphite brushes and a split ring commutator.

Fig. 2 shows an electrical model of a brushed DC motor. In this figure, $V(t)$ is the applied voltage, $I(t)$ is the armature current, $R$ is the electrical resistance of the winding, $\Omega(t)$ is the motor speed, and $Q_m(t)$ is the motor torque. The inductance, $L$, and the voltage source, $E(t)$, stem from Faraday's law, which relates the voltage induced in a coil of wire to the magnetic flux linked by that coil. The voltage source, $E(t)$, is termed the *back electromotive force* (bEMF). For a brushed DC motor, the motor torque is proportional to the armature current and the bEMF is proportional to the motor speed. These relationships are given by

$$Q_m(t) = K_t I(t), \tag{5a}$$

$$E(t) = K_e \Omega(t), \tag{5b}$$

where $K_t$ is the motor torque constant and $K_e$ is the electromotive force constant. Assuming the electrical power in the bEMF is entirely converted into mechanical power, it is easy to show that $K_t = K_e$.

The brushless DC (BLDC) motor is more complex than its brushed counterpart. A typical BLDC has three phase windings, which may be connected in a wye or delta configuration. The field is created by a permanent magnet, which is fixed to the rotor. Each phase winding produces torque and generates a bEMF. For an individual winding, the torque to current ratio and the bEMF to speed ratio are no longer constants, as in (5). Instead, these ratios depend on the angular position of the rotor. The windings of a BLDC motor are commutated via electronic switches, as opposed to mechanical means. The electronic switches are found on the electronic speed controller (ESC). The ESC performs the role of the commutator in a brushed motor: it reverses polarity and interrupts current flow.

Despite the complexities of the BLDC, it can be shown that (5a) still applies for the overall motor/ESC combination, provided the appropriate commutation scheme is employed. In other words, the total motor torque is proportional to the

DC command current drawn by the ESC [p. 55] [25]. For this reason, the brushed DC motor model approximately resembles that of a BLDC/ESC combination [25], [26]. As such, we appropriate the brushed DC motor model of Fig. 2 for the UAV's powertrain. We note that this substitution has precedence in the literature [27], [28].

A useful result is the relationship between motor torque and motor speed:

$$Q_m(t) = \frac{K_t}{R}\big(V(t) - K_e\Omega(t)\big). \tag{6}$$

This result is obtained by applying Kirchhoff's voltage law to the circuit of Fig. 2 and using the motor relations of (5). This result assumes the voltage drop across the inductor is negligible.

*3) Propeller Theory:* A model for the propeller torque may be obtained using dimensional analysis. Suppose $Q$ is the propeller torque [N·m], $D$ is the propeller diameter [m], $\Omega$ is the propeller speed [rad/s], $u$ is the flight speed [m/s], $\rho$ is the fluid density [kg/m$^3$], $\nu$ is the fluid viscosity [m$^2$/s], and $K$ is the fluid volume modulus [N/m$^2$]. These quantities are the physically relevant variables for the propeller torque problem. As such, they are related via an unknown function of the form

$$F(Q, D, \Omega, u, \rho, \nu, K) = 0. \tag{7}$$

Using dimensional analysis, it is possible to express (7) in terms of the following dimensionless $\pi$ groups:

$$\pi_1 = \frac{Q}{\rho\Omega^2 D^5}, \quad \pi_2 = \frac{u}{\Omega D}, \quad \pi_3 = \frac{\Omega D^2}{\nu}, \quad \pi_4 = \frac{\rho\Omega^2 D^2}{K}.$$

The dimensionless variables $\pi_2$, $\pi_3$ and $\pi_4$ are equivalent to the advance ratio, $\lambda$, the Reynolds number, $R_e$, and the Mach number, $M_a$, respectively. Using these $\pi$ groups, (7) may be rewritten as

$$\frac{Q}{\rho\Omega^2 D^5} = C_Q(\lambda, R_e, M_a)$$

The right-hand-side of the previous equation is called the *torque coefficient* and is denoted by $C_Q$. Thus, we have

$$Q = C_Q\rho\Omega^2 D^5, \tag{8}$$

where $C_Q$ is a function of the advance ratio, the Reynolds number, and the Mach number.

*4) Model of the Current-Induced Magnetometer Bias:* Having reviewed the required background, the transfer function from the throttle command, $\delta_t$, to the current-induced bias, $\vec{B}$, may now be established. The throttle command is directly proportional to the motor speed, $\Omega$, and is given by

$$\delta_t = \Omega/\Omega_{\max}, \tag{9}$$

where $\Omega_{\max}$ is the maximum speed of the motor. It follows that $0 \leq \delta_t \leq 1$. Equation (9) assumes the ESC's response function is linear. (This assumption will be revisited in the results section.) The relationship between $\Omega$ and the propeller torque, $Q$, is given by (8). Under dynamic equilibrium, the motor torque, $Q_m$, matches $Q$. This torque matching condition is expressed graphically in Fig. 3. In this figure, $Q$ varies with $\Omega$ according to (8) and $Q_m$ varies with $\Omega$ according to (6).

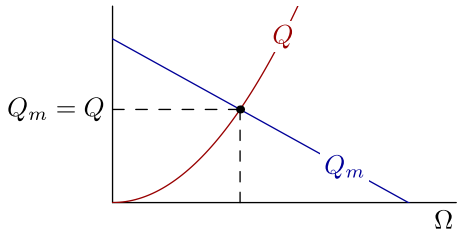


Fig. 3. Under dynamic equilibrium, the motor torque, $Q_m$, matches the propeller torque, $Q$.

The relationship between $Q_m$ and the current, $I$, is given by (5a) and the relationship between $I$ and the magnetometer bias, $\vec{B}$, is given by (4). Combining all the previous relationships, the following model is obtained:

$$\vec{B} = \frac{C_Q\rho(\delta_t\Omega_{\max})^2 D^5}{K_t}\frac{\mu_0}{4\pi}\int\frac{d\vec{s}\times\vec{r}}{r^3}. \tag{10}$$

This equation shows the current-induced bias is proportional to the square of the throttle command:

$$\vec{B} = \delta_t^2\vec{\theta}. \tag{11}$$

The parameter vector $\vec{\theta} \in \mathbb{R}^3$ groups all the unknown coefficients in (10). This parameter vector will be determined using a parameter estimator, as shown in the next section.

## C. Parameter Estimators

Assuming the linear and time-invariant sensor errors have been properly canceled, the only error that remains is the current-induced bias. Thus, the measurement model becomes

$$\vec{v} = \vec{u} + \delta_t^2\vec{\theta}. \tag{12}$$

Suppose the attitude of the sensor is parameterized by the body-to-earth rotation matrix $R = R_b^e$. Solving (12) for $\vec{u}$ and rotating the result into the earth's reference frame yields

$$\vec{u}^{\,e} = R\left(\vec{v} - \delta_t^2\vec{\theta}\right), \tag{13}$$

where $\vec{u}^{\,e}$ is the magnetic field vector expressed in the earth's reference frame. Over several tens of miles, $\vec{u}^e$ will be approximately constant. The NOAA maintains magnetic maps which evaluate $\vec{u}^{\,e}$ based on a zip code.[1]

*1) Offline Estimation:* If the vehicle is stationary, $\vec{\theta}$ can be estimated using a least squares estimator. Because the vehicle is stationary, the field vector $\vec{u}$ is constant and may be designated as an unknown parameter. The $x$ component of (12) may be written as

$$v_x = \begin{bmatrix}\delta_t^2 & 1\end{bmatrix}\begin{bmatrix}\theta_x \\ u_x\end{bmatrix}.$$

The $y$ and $z$ components of (12) may be expressed similarly. The previous equation is of the form $\vec{y} = X\vec{\beta}$, which enjoys the least squares solution. The least squares estimator and the covariance of the estimator are [29]

$$\hat{\beta} = (X^T X)^{-1} X^T \vec{y}, \tag{14a}$$

$$P = \left(X^T X\right)^{-1}\sigma^2, \tag{14b}$$

[1] www.ngdc.noaa.gov/geomag/calculators/magcalc.shtml

where $\sigma^2$ is the variance of the noise. An estimate of the noise variance is given by

$$\hat{\sigma}^2 = \frac{(\vec{y} - X\hat{\beta})^T(\vec{y} - X\hat{\beta})}{n - p}, \tag{15}$$

where $n$ is the number of observations and $p$ is the number of parameters.

*2) Online Estimation:* The previous estimation scheme works only if the vehicle is stationary; that way, any change in the magnetometer reading is due to a change in the current. To determine the parameters in realtime and while the vehicle is moving, we adapt the nonlinear observer designed by Troni and Whitcomb in [19] to incorporate our model for the current induced magnetometer bias. First, (13) is differentiated to produce

$$0 = \dot{R}\left(\vec{v} - \delta_t^2\vec{\theta}\right) + R\left(\dot{\vec{v}} + 2\delta_t\dot{\delta}_t\vec{\theta}\right). \tag{16}$$

Let $\vec{\omega}$ be the angular velocity vector and let $\vec{\omega}_\times$ be the skew symmetric cross product matrix defined as

$$\vec{\omega}_\times \equiv \begin{bmatrix} 0 & -\omega_3 & \omega_2 \\ \omega_3 & 0 & -\omega_1 \\ -\omega_2 & \omega_1 & 0. \end{bmatrix} \tag{17}$$

The kinematics of the rotation matrix $R$ are given by the strap-down equation [30]:

$$\dot{R} = R\vec{\omega}_\times. \tag{18}$$

Using the strap-down equation and assuming the throttle command is held constant, (16) can be rearranged to yield

$$\dot{\tilde{v}} = -\omega_\times\left(\vec{v} - \delta_t^2\vec{\theta}\right). \tag{19}$$

The observer dynamics are defined as

$$\dot{\hat{v}} = -\omega_\times\left(\hat{v} - \delta_t^2\hat{\theta}\right) - k_1\tilde{v}, \tag{20a}$$

$$\dot{\hat{\theta}} = k_2\delta_t^2\omega_\times\tilde{v}, \tag{20b}$$

where the estimation errors are defined as $\tilde{v} \equiv \hat{v} - \vec{v}$ and $\tilde{\theta} \equiv \hat{\theta} - \vec{\theta}$. Given an angular rate signal, $\vec{\omega}$, and a biased field vector measurement, $\vec{v}$, the goal of the observer is to drive the estimation error to zero, *i.e.* $\tilde{\theta} \to 0$. The proposed observer satisfies this goal, as shown by the following stability analysis. The proof relies on the following definition and lemma.

*Definition 1 (Persistently Exciting [31]):* *A matrix function $\mathcal{W} : \mathbb{R}^+ \to \mathbb{R}^{m\times m}$ is persistently exciting (PE) if there exists $T, \alpha_1, \alpha_2 > 0$ such that for all $t \geq 0$:*

$$\alpha_1 I_m \geq \int_t^{t+T} \mathcal{W}(\tau)\mathcal{W}^T(\tau)d\tau \geq \alpha_2 I_m. \tag{21}$$

*Lemma 1:* *Given a system of the following form*:

$$\dot{e}_1 = g(t)e_2 + f_1(t); \quad e_1 \in \mathbb{R}^p,$$
$$\dot{e}_2 = f_2(t),$$

*such that*

*(i)* $||e_1(t)|| \to 0$, $||f_1(t)|| \to 0$, *and* $||f_2(t)|| \to 0$ *as* $t \to \infty$,

*(ii)* $g(t), \dot{g}(t)$ *are bounded, and* $g^T(t)$ *is persistently exiting; then* $\lim_{t\to\infty} ||e_2(t)|| = 0$.

*Proof:* See [31] for proof. □

*Theorem 1:* *Consider the system (19) for time-varying $\vec{\omega}(t)$ and $\vec{v}(t)$. Assume that $\vec{\omega}(t)$, $\dot{\vec{\omega}}(t)$ and $\vec{v}(t)$ remain bounded for all time. Also assume that $\vec{\omega}(t)$ is persistently excited. Let $(\hat{v}, \hat{\theta})$ denote the solution to (20) with $k_1, k_2 > 0$. Then the equilibrium point $(\tilde{v}, \tilde{\theta}) = (0, 0)$ is globally asymptotically stable.*

*Proof:* From (20), the error dynamics are derived to be

$$\dot{\tilde{v}} = -\omega_\times\left(\tilde{v} - \delta_t^2\tilde{\theta}\right) - k_1\tilde{v}, \tag{22a}$$

$$\dot{\tilde{\theta}} = k_2\delta_t^2\omega_\times\tilde{v}. \tag{22b}$$

Define a candidate Lyapunov function by

$$V = \frac{1}{2}\tilde{v}^T\tilde{v} + \frac{1}{2k_2}\tilde{\theta}^T\tilde{\theta}. \tag{23}$$

Note the Lyapunov function is positive definite and radially unbounded. The derivative of $V$ is given by

$$\begin{aligned}\dot{V} &= \tilde{v}^T\dot{\tilde{v}} + \frac{1}{k_2}\tilde{\theta}^T\dot{\tilde{\theta}}, \\ &= \tilde{v}^T\left[-\omega_\times\left(\tilde{v} - \delta_t^2\tilde{\theta}\right) - k_1\tilde{v}\right] + \frac{1}{k_2}\tilde{\theta}^T\left(k_2\delta_t^2\omega_\times\tilde{v}\right), \\ &= -\tilde{v}^T\omega_\times\tilde{v} + \delta_t^2\tilde{v}^T\omega_\times\tilde{\theta} - k_1\tilde{v}^T\tilde{v} + \delta_t^2\tilde{\theta}^T\omega_\times\tilde{v}, \\ &= -k_1\tilde{v}^T\tilde{v} \leq 0.\end{aligned}$$

Because $\dot{V} \leq 0$, it follows that $V \in \mathcal{L}_\infty$. Because $V$ is radially unbounded, it follows that $\tilde{v}, \tilde{\theta} \in \mathcal{L}_\infty$. Because $\vec{\omega} \in \mathcal{L}_\infty$ (by assumption), it follows that $\dot{\tilde{v}}, \dot{\tilde{\theta}} \in \mathcal{L}_\infty$ by (20). Since $\tilde{v}, \tilde{\theta} \in \mathcal{L}_\infty$ and $\dot{\tilde{v}}, \dot{\tilde{\theta}} \in \mathcal{L}_\infty$, it follows that $\tilde{v}$ and $\tilde{\theta}$ are uniformly continuous. Furthermore, $\tilde{v} \in \mathcal{L}_2$ since

$$\left[\int_0^\infty \tilde{v}^T(\tau)\tilde{v}(\tau)d\tau\right]^{1/2} \leq \left[\frac{1}{k_1}V(0)\right]^{1/2}.$$

Thus, from Barbalat's lemma [32], $\tilde{v}$ is globally asymptotically stable at the origin, *i.e.* $\tilde{v} \to 0$. Because $\tilde{v} \to 0$ and $\delta_t, \vec{\omega} \in \mathcal{L}_\infty$, it follows from (20b) that $\dot{\tilde{\theta}} \to 0$. Furthermore, because $\vec{\omega}$ is persistently exciting and $\vec{\omega}, \dot{\vec{\omega}}$ are bounded, we conclude from lemma 1 that $\lim_{t\to\infty}\tilde{\theta} = 0$. □

### D. Hardware and Implementation

Fig. 4 shows the aerial vehicle used to test the theory and algorithms presented previously. The platform is a tailless delta wing that is driven by a pusher propeller and actuated by two elevons. The fins, elevons and motor-mount are manufactured in-house; the foam airframe and the remaining components are off-the-shelf. The aircraft has a wingspan of 37 inches, weighs less than 18 ounces, and can fly continuously for 30 minutes. The delta wing has been used in our group for over a decade for a variety of missions, including wireless communication characterization [33], [34], cooperative control [35], and atmospheric sensing [36].

The vehicle is controlled by the AMP autopilot, which is made in-house by our research group [37]. The autopilot is a collection of electronic devices, namely a GPS receiver, a radio transceiver, a barometer, an atmospheric sensor, and an IMU. Processing is done using a 16 bit, 140 MHz microprocessor.

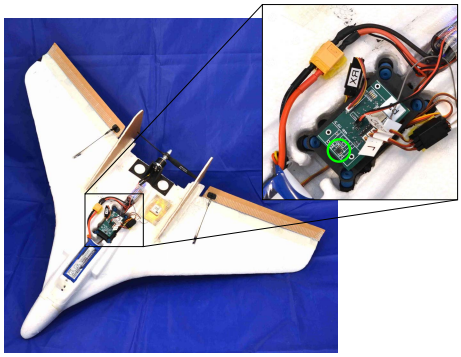

Fig. 4. A battle-tested delta wing UAV. The inset shows a close-up of the autopilot. Note the proximity of the IMU (green circle) to the battery's power leads.

The microprocessor belongs to the DSPIC33 family of microprocessors made by Microchip. Additionally, an Xbee radio can plug into headers on the underside of the board. Along the perimeter of the board is a header that breaks out all the unassigned pins of the microcontroller. Additional sensors can be wired into this header for mission-specific customization of the autopilot.

The IMU is the MPU-9250 made by Invensense; it combines a gyroscope triad, an accelerometer triad, and a magnetometer triad. The magnetometer is a Hall effect sensor. The Hall effect describes the voltage induced by a current moving through a flat conductor in the presence of a magnetic field [p. 867] [24]. The magnetometer has a built-in, 16 bit ADC and a resolution 1.5 mG/LSB.

The adaptive observer is implemented in C and is executed by the autopilot's microprocessor at a rate of 25 Hz. The inputs to the observer are the measurements from the gyroscope triad, the measurements from the magnetometer triad, and the throttle command. In order to improve the signal to noise ratio, a digital, low-pass filter with a corner frequency of 5 Hz is applied to the magnetometer readings upstream of the adaptive observer.

To better discuss the results presenting next, it helps to establish how much error in the estimated yaw angle is acceptable/reasonable. Acceptable error limits based on application vary greatly and will not be considered. On the other hand, acceptable error limits based on the accuracy of the hardware can be easily adapted to different applications. The following calculation shows how the uncertainty in the magnetometer measurement propagates to the uncertainty in the estimated yaw angle. The attitude estimator is approximated by

$$\psi = -\text{atan}(m_y/m_x), \tag{24}$$

where $m_x$ and $m_y$ are the magnetometer measurements with respect to the $x$ and $y$ axes of the vehicle-fixed reference frame. This equation assumes the vehicle is restricted to the horizontal plane and the magnetic field is pointing directly north. Let $\sigma_m^2$ represent the variance of both $m_x$ and $m_y$. Using the propagation of error formula, the variance of the yaw angle is given by

$$\sigma_\psi^2 = \frac{\sigma_m^2}{m_x^2 + m_y^2}.$$

A simple coordinate transformation shows that $m_x = H\cos\psi$ and $m_y = H\sin\psi$ where $H$ denotes the magnitude of the earth's magnetic field. It follows that $\sigma_\psi = \sigma_m/H$. Specializing to our geographic location and our hardware, we get that $H = 0.464$ mG and $\sigma_m = 0.0082$ mG. It follows that the $3\sigma$ error bound is 3°.

The previous analysis assumes the sensor errors are limited to just measurement noise and the attitude estimator is approximated by (24). Given these simplifying assumptions, the 3° error limit should be interpreted more as a ballpark figure than a strict requirement.

## III. Results

This section presents the experimental results. The results are organized into three parts. In the first part, the DPI method is used to calibrate the magnetometers of two AMP autopilots. The first autopilot is embarked on the aerial vehicle shown in Fig. 4. The magnetometer of the second autopilot is used as a reference for subsequent tests. In the second part, the current-induced bias model (11) is experimentally verified. Furthermore, the model parameters are estimated using the offline approach and the online approach. In the third part, we show that the proposed observer is able to identify the current-induced bias and cancel its negative effects.

### A. Basic Calibration

The first step is to calibrate the magnetometers on both the vehicle autopilot and reference autopilot. The magnetometers are calibrated using the DPI method; the reference down direction is taken to be the last column of the earth-to-body rotation matrix. The gyroscope measurements are fused into the attitude estimate at 100 Hz and the accelerometer measurements are fused at 25 Hz. Fusing the accelerometer at a slower rate makes the reference vector less susceptible to sensor errors (*i.e.* scaling factor errors and inertial accelerations). To generate the calibration data, the vehicle is rotated by hand while the autopilot downlinks magnetometer data and observations of the reference "down" vector. At minimum, we collect 10K observations. For best results, the measurements should be uniformly distributed over the sensor's response surface. As proved in [10], the response surface of an uncalibrated magnetometer is an off-centered ellipsoid; the response surface of a calibrated magnetometer is a sphere centered at the origin. Fig. 5 shows the loci of magnetometer measurements before and after calibration. Qualitatively, it is clear that the calibration produces the desired result (*i.e.* a centered sphere). Fig. 5 corresponds to the vehicle autopilot; a similar result is obtained for the reference autopilot. That is, the response surface of the reference magnetometer goes from a shifted ellipsoid to a centered sphere.

To verify the magnetometer calibration quantitatively, a simple compass rose is printed on a piece of paper and taped to a level surface. Using a recreational field compass, the compass rose is aligned to true north (taking into account the local magnetic declination). The autopilots are then pointed in the four cardinal directions of the compass rose. The estimated yaw angles are recorded in Table I.

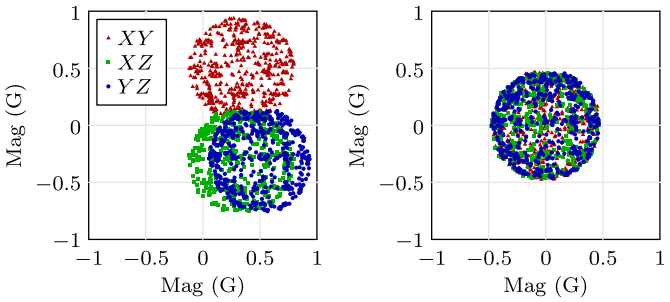


Fig. 5. Locus of magnetometer measurements, before calibration (left) and after calibration (right).

TABLE I
MAGNETOMETER ACCURACY RESULTS

| Direction | Expected | Vehicle | Reference |
|---|---|---|---|
| North | 0 | 0.0 | 0.1 |
| East | 90 | 92.6 | 90.6 |
| South | ±180 | 180.0 | -177.3 |
| West | -90 | -91.4 | -88.3 |

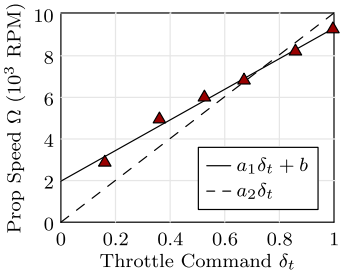


Fig. 6. Propeller speed versus throttle command. A freshly charged battery is used for each observation.

## B. Model Verification and Parameter Estimation

Here, we test the validity of the linear relationship between throttle command and motor speed, *i.e.* (9). Using a handheld tachometer, the speed of the motor/propeller is measured for various throttle settings. A fresh battery is used for each observation. This is done to reduce the effect of battery drainage. The data is plotted in Fig. 6, along with two linear models. The first model (solid line) admits an offset whereas the second model (dashed line) passes through the origin. The $R^2$ values for the first and second models are 0.99 and 0.83, respectively. Despite the lower $R^2$ value, the second model is adopted for further evaluation. The first model is not considered because it would make the magnetometer bias model nonlinear in the parameters. (This decision will be revisited in the discussion section).

Next, we estimate the model parameters. As described in the methods section, the parameters may be determined using an offline approach or an online approach. The offline approach requires the vehicle to be stationary, which allows the parameters to be determined using least squares. Fig. 7 shows the results of the offline approach. The magnetometer signals are recorded while the throttle is increased from 0 to 100%. The bias model (11) is fit to the data using (14a) and the variance of the measurement noise is estimated using (15).

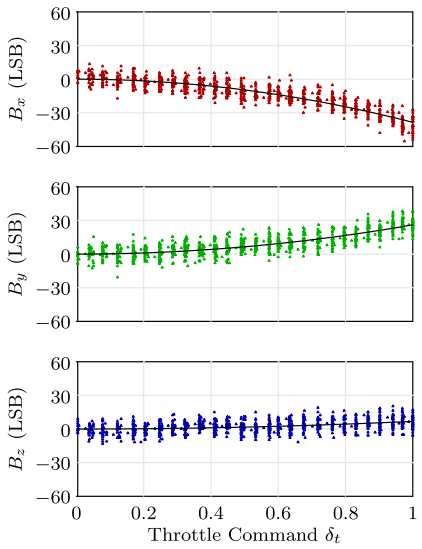


Fig. 7. Magnetometer bias versus throttle command. $B_x$, $B_y$, and $B_z$ denote the components of the magnetometer bias, $\vec{B}$. The model parameters can be easily determined if the vehicle is stationary. Then, any change in the magnetometer signal is due to a change in throttle.

TABLE II
RESULTS OF OFFLINE APPROACH

| Axis | $\theta$ (LSB) | $\hat{\sigma}$ (LSB) | $R^2$ | SNR (dB) | Benchmark $R^2$ |
|---|---|---|---|---|---|
| $x$ | -40.7 | 5.3 | 0.85 | 17.7 | $0.849 \pm 0.013$ |
| $y$ | 17.6 | 5.4 | 0.50 | 10.2 | $0.503 \pm 0.039$ |
| $z$ | -0.8 | 5.6 | 0.00 | -17.0 | $0.002 \pm 0.006$ |

Additionally, the $R^2$ value and the signal-to-noise ratio (SNR) are also computed. In this case, the signal is assumed to be the coefficient of the bias model. A benchmark for the $R^2$ values is generated via a Monte-Carlo simulation. The Monte-Carlo simulation assumes the underlying model is quadratic and the noise is additive, zero mean and normally distributed. The variance of the simulated noise matches the variance of the measurement noise. Table II lists the results of the offline approach. The benchmark $R^2$ values are listed with their $2\sigma$ error bounds.

The calibration coefficients may also be determined using the online adaptive estimator. For this test, the throttle is set to full throttle and the vehicle is rotated by hand, thus satisfying the persistently exciting condition on $\vec{\omega}(t)$. This test is similar to the basic calibration test, except that the propeller is spinning at several thousand RPM. The parameter estimates are shown in Fig. 8. The horizontal lines show the parameter estimates as determined by the offline method.

## C. Yaw Angle Recovery

The final step is to verify that accurate yaw tracking is recovered when the estimated current-induced magnetometer bias, $\hat{B}$, is subtracted from the magnetometer readings. The variable of interest is the yaw error. If the orientation of the vehicle is fixed, the yaw error is the change in the estimated yaw angle due to throttle. If the orientation of the vehicle is not fixed, the yaw error is the difference between the yaw angle

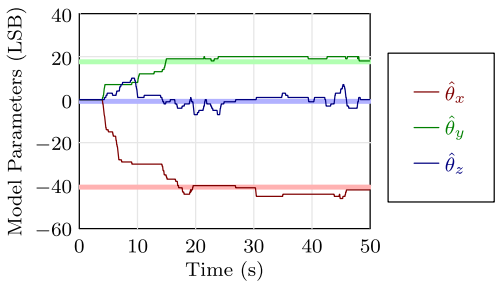


Fig. 8. Parameter estimates over time. The parameter vector, $\hat{\theta}$, comprises the components $\{\hat{\theta}_x, \hat{\theta}_y, \hat{\theta}_z\}$. The "true" parameters, drawn as the thick horizontal lines, are obtained using the offline procedure.

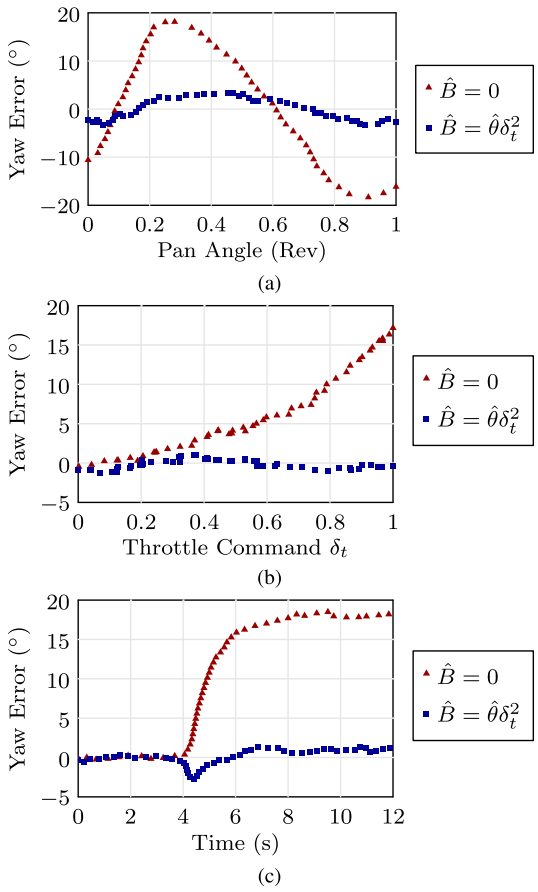


Fig. 9. The ability of the bias model to reduce yaw error is tested under three scenarios: (a) the throttle is set to full and the vehicle is panned in the horizontal plane, (b) the vehicle's orientation is fixed and the throttle is slowly ramped up, and (c) a step input is applied to the throttle at $t = 4$ s.

as estimated by the vehicle autopilot and the yaw angle as estimated by the reference autopilot. The reference autopilot is fixed to the wing tip of the airframe, far enough away from the powertrain to be unaffected by the current.

The yaw error is affected by various factors, such as the orientation of the vehicle with respect to the Earth's magnetic field, the magnitude of the throttle command, and the rate of change of the throttle command. Thus, a proper investigation requires the bias model to be tested under various scenarios. For this study, three scenarios are selected (Fig. 9). For a given scenario, the yaw error is plotted with the bias model disabled, $\hat{B} = 0$, and enabled, $\hat{B} = \hat{\theta}\delta_t^2$.

TABLE III
MAXIMUM YAW ERROR

| Scenario | No Correction | With Correction |
|---|---|---|
| Vehicle Pan | 18.6° | 3.7° |
| Throttle Ramp | 17.2° | 1.3° |
| Throttle Step | 18.5° | 2.8° |

The first scenario (Fig. 9a) considers the effect of vehicle orientation on yaw error. For this test, the throttle is set to full throttle and the vehicle—with the reference autopilot attached to the wingtip—is panned in the horizontal plane. The second scenario (Fig. 9b) considers the effect of throttle magnitude. Here, the vehicle's orientation is fixed and the throttle is slowly ramped up from 0 to 100%. The third scenario (Fig. 9c) considers the effect of throttle rate of change. Like the previous test, the vehicle's orientation is fixed. A step input is applied to the throttle at $t = 4$ s. Table III lists the maximum yaw error across all three scenarios.

## IV. Discussion & Concluding Remarks

In this section, we begin by interpreting our results and drawing key conclusions. Following this, we summarize our findings. Finally, we discuss some practical applications of this work.

Beginning with the basic calibration results, we note the estimation error is less than 3° (see Table I). This precision is remarkable considering the calibration was *in-situ*, the accelerometers were uncalibrated and the platforms were rotated by hand. We also note that this error is consistent with the error analysis presented in Section II-D.

The throttle model verification experiment (Fig. 6) compares two competing models. The first model admits an offset whereas the second model passes through the origin. Through experience, we expect the first model to be more accurate, since it typically takes two or three clicks of the throttle stick for the motor to start spinning. The empirical $R^2$ values corroborate our experience. A possible explanation for the offset is that a start-up current is needed to overcome the friction of the motor. Another explanation is that the ESC has trouble sensing the bEMF of the unused phase a low speeds. Regardless of the cause, the offset presents a complication—it makes the magnetometer bias model nonlinear in the parameters. Fortunately, the offset may not be necessary: the error associated with neglecting the offset is negligible when compared to the measurement noise, as shown by the next experiment. For this reason, we deem the second model, which corresponds to (9), to be sufficiently accurate for our needs.

Turning to the offline approach, we note the measurement noise is substantial, as borne out by the computed SNRs (see Table II). The $R^2$ values differ greatly, but positively correlate to the SNRs. The Monte-Carlo simulation, which assumes the underlying model is quadratic, produces $R^2$ values which agree with the experimental values. This agreement supports the hypothesis that a quadratic model is appropriate for the current-induced magnetometer bias.

We note the offline approach has limited usefulness because the vehicle is required to be stationary. However, it provides

a benchmark for the online approach. Fig. 8 shows the online approach arriving at parameter values similar to those obtained with the offline approach. The online parameters, however, feature minor fluctuations. A possible explanation for these fluctuations is that the online approach ignores measurement noise. We expect the noise to produce a bounded error in the estimated parameters.

Ultimately, the purpose of the parameter estimation is to fix the yaw attitude. Consequently, errors in the estimated parameters are tolerable provided the yaw attitude is sufficiently accurate. The ability of the bias model to correct yaw errors is demonstrated by the experiments shown in Fig. 9. The bias model is able to reduce the yaw error across all yaw angles (Fig. 9a), throttle settings (Fig. 9b), and for a step input to the throttle command (Fig. 9c). As shown in Table III, the bias model is able to reduce the maximum error by a factor of 5 or greater, when compared to the case of no bais correction. Furthermore, the maximum yaw errors are reasonable, given the uncertainty analysis presented in Section II-D and the benchmark yaw errors listed in Table I.

In summary, we have developed a way to fix current-induced magnetometer biases. First, we demonstrated that repeatable, straightforward, *in-situ* magnetometer calibration is possible when the right source for the reference vector is selected. By combining knowledge of electomagnetism, electric motors, and propeller aerodynamics, we established a model for the current-induced magnetometer bias as a function of the throttle command. Finally, we designed an adaptive estimator to determine the model parameters in realtime. The advantage of our method over existing techniques is the ability to handle rapid changes in throttle command. Existing adaptive estimators assume the bias is constant [18], [19]. Thus, a change in throttle would shift the equilibrium point of the estimator. However, because we are estimating a set of model parameters (as opposed to the bias directly), our approach can handle rapid changes in the throttle command. Furthermore, the quasi-static assumption is more applicable to a set of model parameters than to the bias itself.

The primary application of this work is vehicle state-estimation. Because of their sensitivity to unwanted magnetic sources (*i.e.* hard irons, soft irons and currents), magnetometers have often been dismissed as a lost cause. As an alternative, the yaw angle is taken to be the course-over-ground (COG) reading from a GPS unit. However, for low speeds or GPS denied environments, the COG signal is no longer available. Also, for vehicles that side-slip significantly, the COG is a poor substitute for the yaw angle. Finally, GPS suffers from slow refresh rates. For these reasons, the magnetometer is preferable to GPS as a yaw attitude sensor. Our hope is that, because of this work, roboticists will come to rely on the magnetometer for navigation, much like the mariners of old came to rely on the compass.

## REFERENCES


[1] M. Guarnieri, "Once upon a time...The compass," *IEEE Ind. Electron. Mag.*, vol. 8, no. 2, pp. 60–63, Jun. 2014.

[2] M. D. Shuster and S. D. Oh, "Three-axis attitude determination from vector observations," *J. Guid. Control, Dyn.*, vol. 4, no. 1, pp. 70–77, 1981.

[3] J. D. Barton, "Fundamentals of small unmanned aircraft flight," *Johns Hopkins APL Tech. Dig.*, vol. 31, no. 2, pp. 132–149, 2012.

[4] G. Lerner and M. D. Shuster, "In-flight magnetometer calibration and attitude determination for near-earth spacecraft," *J. Guid. Control*, vol. 4, no. 5, pp. 518–522, 1981.

[5] R. Alonso and M. D. Shuster, "TWOSTEP: A fast robust algorithm for attitude-independent magnetometer-bias determination," *J. Astron. Sci.*, vol. 50, no. 4, pp. 433–451, 2002.

[6] R. Alonso and M. D. Shuster, "Complete linear attitude-independent magnetometer calibration," *J. Astron. Sci.*, vol. 50, no. 4, pp. 477–490, 2002.

[7] J. L. Crassidis, K.-L. Lai, and R. R. Harman, "Real-time attitude-independent three-axis magnetometer calibration," *J. Guid., Control Dyn.*, vol. 28, no. 1, pp. 115–120, 2005.

[8] D. Gebre-Egziabher, "Magnetometer autocalibration leveraging measurement locus constraints," *J. Aircr.*, vol. 44, no. 4, pp. 1361–1368, Jul. 2007.

[9] C. C. Foster and G. H. Elkaim, "Extension of a two-step calibration methodology to include nonorthogonal sensor axes," *IEEE Trans. Aerosp. Electron. Syst.*, vol. 44, no. 3, pp. 1070–1078, Jul. 2008.

[10] J. F. Vasconcelos *et al.*, "Geometric approach to strapdown magnetometer calibration in sensor frame," *IEEE Trans. Aerosp. Electron. Syst.*, vol. 47, no. 2, pp. 1293–1306, Apr. 2011.

[11] Y. Wu and S. Luo, "On misalignment between magnetometer and inertial sensors," *IEEE Sensors J.*, vol. 16, no. 16, pp. 6288–6297, Aug. 2016.

[12] M. Zhu, Y. Wu, and W. Yu, "An efficient method for gyroscope-aided full magnetometer calibration," *IEEE Sensors J.*, vol. 19, no. 15, pp. 6355–6361, Apr. 2019.

[13] M. Kok, J. D. Hol, T. B. Schön, F. Gustafsson, and H. Luinge, "Calibration of a magnetometer in combination with inertial sensors," in *Proc. 15th Int. Conf. Inf. Fusion*, Singapore, Jul. 2012, pp. 787–793.

[14] M. Kok and T. B. Schön, "Magnetometer calibration using inertial sensors," *IEEE Sensors J.*, vol. 16, no. 14, pp. 5679–5689, Jul. 2016.

[15] G. Troni and R. M. Eustice, "Magnetometer bias calibration based on relative angular position: Theory and experimental comparative evaluation," in *Proc. IEEE/RSJ Int. Conf. Intell. Robots Syst.*, Chicago, IL, USA, Sep. 2014, pp. 444–450.

[16] J. Metge, R. Megret, A. Giremus, Y. Berthoumieu, and C. Mazel, "Dynamic magnetic field compensation for micro UAV attitude estimation," in *Proc. Int. Conf. Unmanned Aircr. Syst. (ICUAS)*, Atlanta, GA, USA, May 2013, pp. 725–733.

[17] R. Czyba, W. Janusz, and G. Szafrański, "Compensation of magnetometers error based on nonlinear models for multimotor aerial robots applications," in *Proc. Int. Conf. Unmanned Aircr. Syst. (ICUAS)*, Orlando, FL, USA, May 2014, pp. 885–889.

[18] A. V. Pesterev, Y. V. Morozov, I. V. Matrosov, and J. Ashjaee, "Estimation of the magnetic field generated by UAV in flight," in *Proc. 25th Saint Petersburg Int. Conf. Integr. Navigat. Syst. (ICINS)*, St. Petersburg, Russia, May 2018, pp. 1–4.

[19] G. Troni and L. L. Whitcomb, "Adaptive estimation of measurement bias in three-dimensional field sensors with angular-rate sensors: Theory and comparative experimental evaluation," in *Proc. Robotics, Sci. Syst. Conf. (RSS)*, Berlin, Germany, Jun. 2013, pp. 1–8.

[20] X. Li and Z. Li, "A new calibration method for tri-axial field sensors in strap-down navigation systems," *Meas. Sci. Technol.*, vol. 23, no. 10, pp. 105105-1–105105-6, 2012.

[21] R. Zhang, F. Höflinger, and L. M. Reind, "Calibration of an IMU using 3-D rotation platform," *IEEE Sensors J.*, vol. 14, no. 6, pp. 1778–1787, Jun. 2014.

[22] O. Särkkä, T. Nieminen, S. Suuriniemi, and L. Kettunen, "A multi-position calibration method for consumer-grade accelerometers, gyroscopes, and magnetometers to field conditions," *IEEE Sensors J.*, vol. 17, no. 11, pp. 3470–3481, Jul. 2017.

[23] R. Mahony, T. Hamel, and J.-M. Pflimlin, "Nonlinear complementary filters on the special orthogonal group," *IEEE Trans. Autom. Control*, vol. 53, no. 5, pp. 1203–1218, Jun. 2008.

[24] H. Radi and J. O. Rasmussen, *Principles of Physics: For Scientists and Engineers*. Heidelberg, Germany: Springer, 2013.

[25] J. R. Mevey, "Sensorless field oriented control of brushless permanent magnet synchronous motors," M.S. thesis, Dept. Elect. Comput. Eng., Kansas State Univ., Manhattan, KS, USA, 2009.

[26] J. C. Gamazo-Real, E. Vázquez-Sánchez, and J. Gómez-Gil, "Position and speed control of brushless DC motors using sensorless techniques and application trends," *Sensors*, vol. 10, no. 7, pp. 6901–6947, 2010.

[27] G. Szafranski, R. Czyba, and M. BŁachuta, "Modeling and identification of electric propulsion system for multirotor unmanned aerial vehicle design," in *Proc. Int. Conf. Unmanned Aircr. Syst. (ICUAS)*, Orlando, FL, USA, May 2014, pp. 470–476.
[28] F. Morbidi, R. Cano, and D. Lara, "Minimum-energy path generation for a quadrotor UAV," in *Proc. IEEE Int. Conf. Robot. Autom. (ICRA)*, Stockholm, Sweden, May 2016, pp. 1492–1498.
[29] S. A. Van De Geer, "Least squares estimation," in *Encyclopedia of Statistics in Behavioral Science*, vol. 2. Hoboken, NJ, USA: Wiley, 2005, pp. 1041–1045.
[30] B. L. Stevens and F. L. Lewis, *Aircraft Control and Simulation*, 2nd ed. Hoboken, NJ, USA: Wiley, 2003.
[31] G. Besançon, "Remarks on nonlinear adaptive observer design," *Syst. Control Lett.*, vol. 41, no. 4, pp. 271–280, Nov. 2000.
[32] H. K. Khalil, *Nonlinear Systems*, 3rd ed. Upper Saddle River, NJ, USA: Prentice-Hall, 2002.
[33] A. Shaw and K. Mohseni, "A fluid dynamic based coordination of a wireless sensor network of unmanned aerial vehicles: 3-D simulation and wireless communication characterization," *IEEE Sensors J.*, vol. 11, no. 3, pp. 722–736, Mar. 2011.
[34] A. Bingler and K. Mohseni, "Dual-radio configuration for flexible communication in flocking micro/miniature aerial vehicles," *IEEE Syst. J.*, vol. 13, no. 3, pp. 2408–2419, Sep. 2019.
[35] B. Hodgkinson, D. Lipinski, L. Peng, and K. Mohseni, "Cooperative control using data-driven feedback for mobile sensors," in *Proc. IEEE Int. Conf. Robot. Automat. (ICRA)*, Karlsruhe, Germany, May 2013, pp. 772–777.
[36] M. Silic and K. Mohseni, "Field deployment of a plume monitoring UAV flock," *IEEE Robot. Autom. Lett.*, vol. 4, no. 2, pp. 769–775, Apr. 2019.
[37] A. Bingler and K. Mohseni, "Dual radio autopilot system for lightweight, swarming micro/miniature aerial vehicles," *J. Aerosp. Inf. Syst.*, vol. 14, no. 5, pp. 293–305, 2017.

**Matthew Silic** received the B.S. degree in mechanical engineering from the University of Florida, Gainesville, FL, USA, in 2012. Since 2013, he has been a Graduate Researcher with the Department of Mechanical and Aerospace Engineering, University of Florida.

**Kamran Mohseni** (M'08–SM'12) received the Ph.D. degree in mechanical engineering from the California Institute of Technology (Caltech), Pasadena, CA, USA, in 2000.

After a year as a Postdoctoral Researcher in control and dynamical systems with Caltech, he joined the University of Colorado at Boulder, Boulder, CO, USA, as an Assistant, and an Associate Professor with the Department of Aerospace Engineering Sciences, before moving to Florida as the W.P. Bushnell Endowed Chair with both the Mechanical and Aerospace Engineering Department and the Electrical and Computer Engineering Department, University of Florida, Gainesville, FL, USA. He is the Director of the Institute for Networked Autonomous Systems and an Associate Fellow of the American Institute of Aeronautics and Astronautics.

Dr. Mohseni is a member of the American Society of Mechanical Engineers, the American Physical Society, and the Society for Industrial and Applied Mathematics.